Synthesis and Chemical Functionalization of Neodymium-doped nanoparticles as Nanothermometers in the Second Biological Window.

Lucia Guadalupe De la Cruz Jesús
Master Program in Nanoscience, Materials and Processes: Chemical Technology at the Frontier, 2014-2015
e-mail: luciaguadalupe.delacruz@estudiants.urv.cat

Supervisor: Ph.D. Joan Josep Carvajal Marti
Physics and Crystallography of Materials and Nanomaterials (FiCMA-FiCNA), Universitat Rovira i Virgili
Campus Sescelades, c/.Marcel·lí Domingo, 1 Tarragona, 43007, Spain.

Abstract. 1 to 5 at. % Neodymium-doped monoclinic phase $KGd(WO_4)_2$ and hexagonal phase $NaGdF_4$ nanoparticles were successfully synthesized by the Pechini sol-gel and hydrothermal methods, respectively. Under excitation at 808 nm, the 3 at. % $Nd:KGd(WO_4)_2$ nanoparticles exhibited strong emission bands at 883 nm and 1067 nm in the near infrared region range, corresponding to the $^4F_{3/2} \rightarrow {}^4I_{9/2}$ and $^4F_{3/2} \rightarrow {}^4I_{11/2}$ transitions of Nd^{3+}, respectively. This last emission lies in the second biological window, and shows promising properties for thermal sensing in this range of wavelengths. In fact, the thermal analysis of these nanoparticles indicated a linear ascent behavior of the fluorescence intensity ratio in both strong. Finally, the surface of these nanoparticles was functionalized by silanization using 3-Aminopropyltriethoxysilane as the coupling agent, allowing deagglomerating and dispersing them in an aqueous medium, with sizes around 16 nm. Hence these nanoparticles are promising for nanothermometry applications in the second biological window.

1 INTRODUCTION

During the last years most of the researches have been focus in the study of the luminescence nanothermometry due to the variation of the luminescent properties of luminescent nanoparticles (LNPs) with temperature, which play a crucial role in thermal image applications, where at the same time it has been used in biophotonics, forthcoming diagnosis and therapy procedures.[1-3]

Aside from this important interest, thermal sensing of biosystems is a key part for the simultaneous monitoring of their temperature to found the origin of behavior and therefore early detection and treatment of many diseases, since one of the first signals of any given illness (such as inflammation, hyperthermia, cancer or cardiac problems) is the appearance of thermal singularities.[4]

Nevertheless, the traditional temperature sensors (thermocouples, thermistors and infrared thermometers) could not fulfill the measure requirements in living cells.[5] For instance, thermocouples are unable to measure the temperature inside living cells, since they determine the temperature by the contact, and have a low spatial resolution. Infrared thermometers based on blackbody radiation, from another side, despite they are a non-contact thermometric technique, also allow measuring only the temperature at the surface of the samples, measuring the thermal radiation and knowing the amount of energy emitted by an object, thus, from these measurements the temperature can be determined.[6]

Because of these limitations, the use of temperature sensors that take advantage of the fluorescence properties of nanoparticles have shown great potential due to their operation in non-contact mode and can find two different applications, in cellular imaging and in temperature sensing at the nanoscale.[1,7,8] This form of thermal sensing is becoming a reality with the recent development of nanothermometers (NTMs), which after a proper surface chemical functionalization, can be dispersed in solutions making them compatible with biological systems.[9-12] However, most of these systems have been operating in the visible range[8,13], which limits their penetration depth into a biological tissue to a few millimeters.[14,15]

Therefore, finding an appropriate alternative, which has sufficient emission of signal but also allows for a deeper penetration during in-vivo imaging experiments, is important. Fortunately, two regions have been identified in the near infrared region (NIR) of the electromagnetic spectrum where the absorption of light by the different component of the biological tissue is reduced, the so-called biological windows. Initially, the focus on research was centered at the first biological window (I-BW), that extends from 700 nm to 950 nm.[16,17] At present, focus has shifted to the second biological window (II-BW),[18-19]that extends from 1,000 nm to 1,400 nm. Two water absorption bands at 980 nm and 1500 nm limit this spectral range. Since longer wavelengths are used in the II BW, there is a reduction of the optical scattering if compared to the I-BW. This reduction is considered to lead to an improvement in the resolution of sub-tissue images. In addition, the slight increment in the absorption coefficient caused by water could be compensated by the reduction in the scattering cross section. Thus, it allows for a longer penetration depth than those obtained in the I-BW[19. spectral range. Since longer wavelengths are used in the II BW, there is a reduction of the optical scattering if compared to the I-BW. This reduction is considered to lead to an improvement in the resolution of sub-tissue images. In addition, the slight increment in the absorption coefficient caused by water could be compensated by the reduction in the scattering cross section. Thus, it allows for a longer penetration depth than those obtained in the I-BW. [19]

Today, LNPs with potential applicability in bioimaging in the II-BW are carbon nanotubes CNTs, which have a unique fluorescence emission band that spans up to the whole spectral range of the II-BW, and make them useful for a deep-tissue imaging.[18] However, working with CNTs needs to deal with the difficult synthesis of nanotubes with high fluorescence efficiency, and can generate unwanted thermal loading during the emission process.[20]

Among the most promising material candidates to work in these biological windows we encounter lanthanide-doped LNPs. Trivalent lanthanide (Ln^{3+})-doped nanocrystals (NCs) have attracted great interest due large stokes shifts, narrow emission band widths, long luminescence lifetimes, biocompatibility, and nontoxicity giving rise to potential applications in diverse fields such as bio-imaging [21-27] and solid-state phosphors for displays.[31-33] To date, multifunctional Ln^{3+} doped LNPs that exhibit two or more different properties are highly desirable for many important technological applications such as multifunctional imaging, and simultaneous diagnosis and therapy due to their versatile functionality.[24,34] The Nd^{3+} ion with an absorption around 800 nm is considered a good candidate to achieve efficient emissions in the I- and II-BWs, and significantly improve the penetration depth for deep-tissue imaging due to the NIR emissions around 850–1,100 nm.[35,36] LNPs doped with neodymium can be used to work in both the I-BW and II-BW based on the three main emission channels of Nd^{3+} ions: $^4F_{3/2} \rightarrow {}^4I_{9/2}$, $^4F_{3/2} \rightarrow {}^4I_{11/2}$ and $^4F_{3/2} \rightarrow {}^4I_{13/2}$ that lead to emissions at around 910 nm, 1050 nm, and 1330 nm, respectively.[18] Nd^{3+} ion shows several advantages such as a small thermal loading due to a single de-excitation channel, no excited state absorption, a large transparency over the visible range, a weaker cross-relaxation process, and a long (ms) radiative lifetime.[37-38]

Due to large Stokes shifts and narrow emission peaks, lanthanide ions can be used as multi-probes for biological measurements. Compared to organic dyes and QDs, Ln^{3+}-doped LNPs exhibit some advantages such as limited photo-bleaching, higher chemical stability and long luminescence lifetimes, and most importantly, low optical background noise due to the absence of auto-fluorescence under NIR radiation.[10,27]

It was found that $KGd(WO_4)_2$ that crystallizes in the monoclinic system with space group C2/c[39] provides a strong physical anisotropy with weaker concentration quenching effects, and activated by Ln^{3+} ions shows high efficiency for stimulated emission at low pumping energies with laser diode excitation.[40,41] And also it is reported as an excellent host for lanthanide ions due to its highly thermal and chemically stability.[39,42]

From another side, $NaGdF_4$, in its ß-phase, crystallizes in the hexagonal system with space group P6, and constitutes an excellent host lattice for Ln^{3+} ions.[43-45] In this material, lattice non-radiative losses are minimized because of its low phonon cutoff energy, which consequently increase the photo luminescent quantum yield, especially in up-conversion processes[3,27], and generally results in higher luminescence efficiencies.[8]

Both materials can also be applied as contrast agents for magnetic resonance imaging (MRI) in vivo because of the strong paramagnetism of Gd.[1,45] The results indicated that in the case of $NaGdF_4$, these dual-functional nanoparticles exhibited excellent signal-to-noise ratio, low cytotoxicity, and can be served as a new platform for imaging biological tissues.[46]

In this work, we synthesized and optimize the doping concentration of Nd^{3+} in the two different hosts, $KGd(WO_4)_2$ and $NaGdF_4$, by sol-gel and hydrothermal methods, respectively. We analyzed their spectroscopic properties, and those nanoparticles showing the highest emission efficiency were functionalized by silanization to disperse them in biological compatible fluids. Finally, the thermometric response in the II-BW of those nanoparticles was analyzed.

2 SYNTHESIS AND EXPERIMENTAL TECHNIQUES

2.1 Synthesis of Nd^{3+}:$KGd(WO_4)_2$ nanoparticles by the Pechini sol-gel method.

Powders of K_2CO_3 (Alfa Aesar, 99.0%), Gd_2O_3 and Nd_2O_3 (Aldrich, 99.9%) were used as starting materials to synthesize 1 to 5 at. % Nd^{3+}:$KGd(WO_4)_2$ nanoparticles. Stoichiometric amounts of these compounds were dissolved with the minimum volume of HNO_3 (Labkem, 65%). The solution was maintained at 373 K until the liquid was completely evaporated. After that, powders of $(NH_4)_2WO_4$ (Aldrich, 99.99%) and EDTA (Alfa Aesar, 99.0%) were dissolved with 40 ml of distilled water during 30 minutes at room temperature. This solution was poured in the nitrates generated and was kept for 2 hours at 323 K to allow the complexation reaction to take place. EDTA is used as the organic chelating agent (CA) with molar ratios 0.16, 0.25, 0.5 and 1 in relation with the metals contained by the nanoparticles. This relation is defined as C_M=[EDTA]/[METAL]. The esterification reaction takes place when adding Polyethyleneglycol (Aldrich, m.w. 400) at this solution, mixed at the same temperature for 30 minutes. The molar ratio relation between the complexation agent and the esterification agent is 1:2 EDTA : PEG, and is defined as C_E=[CA]/[PEG]. When mixed together, EDTA and PEG create a rigid net made of polyester able to reduce the segregation of metals which could take place at high temperatures during the process of polymer decomposition. The following step was a pre-calcination at 603 K during three hours to start decomposing the organic resin. Finally, the precursor powder, with a white-yellowish color, was calcined at 1277K for 8 min and then cooled up to 298 K. A scheme of this synthesis process is shown in Figure 1.

2.2 Synthesis of $Nd^{3+:}NaGdF_4$ nanoparticles

1 to 5 at. % Nd^{3+}:$NaGdF_4$ nanoparticles were synthesized using two different hydrothermal methods.

Method A: 0.70 g of NaOH (Prolabo, 97%) and malonic acid (Aldrich, 99%) were dissolved with 50 ml of distilled water until the solution became transparent. After that, NaF (Aldrich, 99%) was added and mixed during 15 min. At the same time, stoichiometric amounts of Gd_2O_3 and Nd_2O_3 (Aldrich, 99.9%) were dissolved with the minimum volume of HNO_3 (Labkem, 65%). The solution was maintained at 373 K until the liquid was completely evaporated and finally we added this nitrates to the solution previously obtained.

Method B: K_2CO_3 (Alfa Aesar, 99.0%), Gd_2O_3 and Nd_2O_3 (Aldrich, 99.9%) were used as starting materials. Stoichiometric amounts of these compounds were dissolved with the minimum volume of HNO_3 (Labkem, 65%). The solution was maintained at 373 K until the liquid was completely evaporated. After that, NaCl (Prolabo, 99%) was dissolved with 8.3 ml of distilled water until completely dissolved. And then, 0.415g of polyacrylic acid (PAA) (Aldrich, m.v. 1,250,00) were dissolved in 8.3 ml of water and 24.9 ml of ethanol (Pure Merck). Then, we added a solution of NH_4HF_2 (Aldrich, 98.5%) in 8,3 ml of distilled water, and added this solution to the nitrates previously obtained and mixed until completely dissolved.

The solutions obtained by both methods were located in 66.6 ml sealed Teflon vessels, and heated at 473 K for 12 hrs. in method A and 6 hrs. in method B. After that the reactor was cooled at room temperature. Finally, the solution was centrifuged and the supernatant removed, followed of washing with distilled water twice and dry the nanoparticles at 353 K for 8 hrs.

A scheme of these two synthesis processes is shown in Figure 1.

2.3 Functionalization of the surface of $Nd:KGd(WO_4)_2$ nanoparticles.

The surface of 5 at. % $Nd:KGd(WO_4)_2$ nanoparticles was chemically functionalized by silanization to make them dispersible in water, according to the results obtained in the luminescence tests. Different amounts of nanoparticles were mixed in a vial with 2.5 ml of 3-Aminopropyltriethoxysilane (APTES) (Aldrich, 99%) and different volumes of water, as listed in Table 1. This solution was left under agitation for 5 hours at room temperature, using a 5 mm micro-tip in a high-power ultrasonic processor. Different conditions of amplification and pulse duration where used in the experiments, summarized in Table 1. The vial was submerged in a water-ice bath in order to minimize the polymerization of APTES due to the increase of temperature during the sonication process. After that the excess of APTES no linked to the surface of the nanoparticles was removed by adding 2.5 ml of ethanol and/or acetone (Pure Merck), depending on the experiment (see Table 1) and ultrasonicated during 5 minutes. This step was repeated several times until the supernatants became colorless. The resulting mixture was centrifuged during 6 min at 800 rpm in order to separate the functionalized nanoparticles by forcing their deposition. Finally, the chemically functionalized nanoparticles were dispersed in 2.5 ml of water using the high-power ultrasonic processor during 30 min to study their deposition time that will allow us estimating their stability in water compatible fluids.

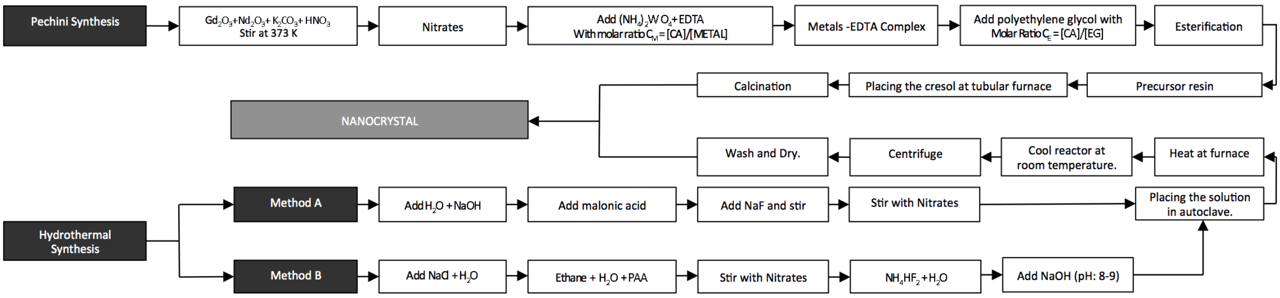

Figure 1. Process scheme used in the synthesis of nanoparticles.

Table 1. Parameters used in the functionalization of nanoparticles.

Sample Name	Time (hrs)	Ultrasound amplification (%)	Ultrasound pulse duration on (s) /off (s)	% vol. Silane -Water	Weight of NPs (mg)	Washing Solvent
Exp 1.	5	20	1/1	100-0	50	Ethanol
Exp 2.	5	30	1/1	100-0	50	Ethanol-Acetone
Exp 3.	5	40	1/1	100-0	50	Acetone
Exp 4.	5	40	1/1	100-0	50	Ethanol
Exp 5.	5	40	1/1	50-50	50	Ethanol
Exp 6.	5	40	1/1	25-75	50	Ethanol
Exp 7.	5	35	1/1	25-75	50	Ethanol
Exp 8.	5	35	2/1	25-75	50	Ethanol
Exp 9.	5	35	3/1	25-75	50	Ethanol
Exp 10	5	35	3/1	25-75	12	Ethanol

2.4 Characterization techniques

X-ray powder diffraction patterns were recorded from the nanoparticles obtained with different dopant concentration and C_M molar ratio using CuKα radiation in a Bruker-AXS D8-Discover diffractometer equipped with a parallel incident beam (Göbel mirror), a vertical θ−θ goniometer, an XYZ motorized stage, and a point detector. The X-ray diffractometer was operated at 40 kV and 40 mA. Identification of the crystalline phases was achieved by comparing the recorded XRD diffractograms with the JCPDS database using the Diffracplus Evaluation software from Bruker.

The particle morphology, and size distribution of the NPs were observed using transmission electron microscopy (TEM) analysis, performed with a JEOL JEM-1011 microscope. The preparation of the samples consisted in placing a drop of the nanopowders, previously mixed in a volatile solvent such as ethanol (Merck, pro analysis 99.8%) or distilled water, on a cooper grid covered by a holey carbon film (HD200 Cooper Form-var/carbon). Ultrasonication was used to reduce and disperse the agglomerates before deposition of the cooper grid. Then, they were drop cast onto the copper grid.

The optical reflectance of the Nd^{3+}:KGd(WO_4)$_2$ and Nd^{3+}:NaGdF_4 nanocrystals was recorded at room temperature using a Varian Cary 500 spectrophotometer. The spectra were recorded from 600 nm to 1000 nm, taking measurements with a data interval of 0.1, SBW of 0.2 and 20 seconds as integration time.

The Nd^{3+} photoluminescence measurements to determine the efficiency of Nd^{3+}-doped materials were carried out at room temperature by a homemade set-up using an 808 nm diode (Ostech) laser as the excitation light source with a power of 1.1 W coupled to an optical fiber and a collimator lens that focuses the light onto an integrating sphere (see Figure 2). The sample was located in a hole of the sphere at 180º of the pumping source and at 90º of the detector. The sphere is covered with a reflective material so when the sample emits light, an optical fiber coupled to the integrating sphere carries the signal to an Yokogawa AQ6373 optical spectrum analyzer (OSA) which acts as photosensor and records the emission spectra. The spectra were recorded from 850 nm to 1400 nm taking measurements every 2 nm.

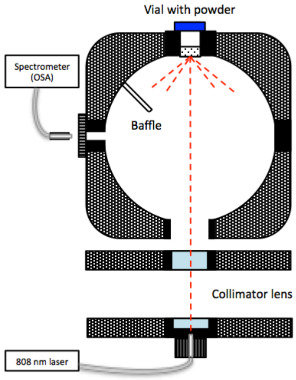

Figure 2. Scheme of the emission measurement setup used to determine the luminescence efficiency of the synthesized nanocrystals.

To determine the variation of the luminescence properties of the 5 at. % Nd^{3+}:KGd(WO_4)$_2$ nanoparticles with temperature, they were introduced in a heating stage (Linkam THMS 600), and their emission was collected in a 90º geometry to minimize the influence of the laser pump on the collected spectra. The pumping source was collimated by a lens, and the emission generated by the sample was again collimated by a lens and also with a microscope objective lens. The spectra were recorded from 850 nm to 1400 nm and taking measurements every 2 nm with the high sensitive mode of the Yokogawa AQ6373 OSA. Figure 3 shows the experimental set-up used to measure the luminescence.

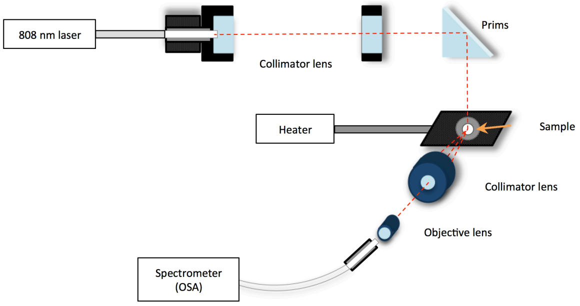

Figure 3. Scheme of the emission measurement setup used to thermometry analyzes.

3 RESULTS AND DISCUSSION

3.1 Structural Characterization

The synthesized nanocrystals were structurally characterized by X-ray powder diffraction. Figure 4 shows the X-ray powder diffraction pattern of the Nd^{3+}:$KGd(WO_4)_2$ nanocrystals, which crystallizes in the monoclinic system with space group C2/c, since all the peaks observed in the experimental pattern could be indexed according to the reference JCPDS 89-8489 pattern[47], also shown in Figure 4.

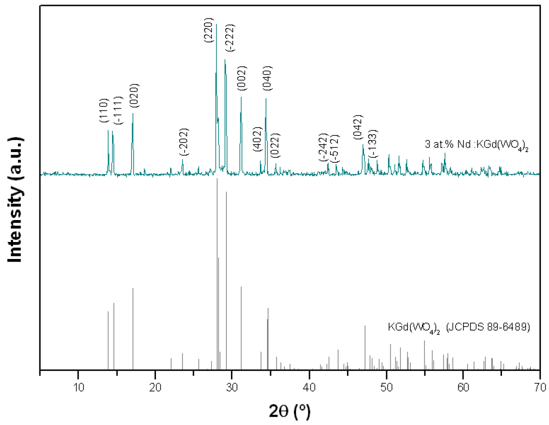

Figure 4. X-ray powder diffraction pattens of monoclinic $KGd(WO_4)_2$ nanocrystals.

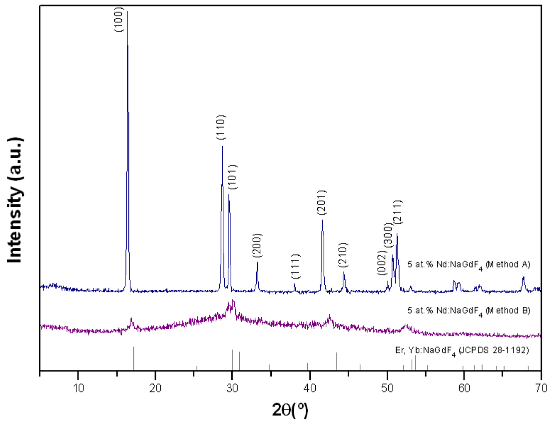

Fligure 5. X-ray powder diffraction pattens of hexagonal $NaGdF_4$ nanocrystals (a) Method A b) Method B

On the other hand, Figure 5 shows the X-ray powder diffraction pattern of the Nd^{3+}:$NaGdF_4$ nanocrystals, which crystallize in the hexagonal system, with space group P6, as can be deduced when compared to the reference JCPDS 28-1192 pattern, corresponding to Er, Yb:$NaYF_4$[48,49], also shown in Figure 5. However, although the diffraction peak positions are in good agreement with the reference data, and no impurities were found, the cristallinity of the material obtained is clearly higher when method A is used for the synthesis of these materials. Furthermore, the important background that can be observed in the X-ray diffraction pattern of Nd^{3+}:$NaGdF_4$ nanocrystals synthesized by method B, indicate the presence of a big amount of amorphous material. Thus, those particles will not be characterized spectroscopically.

3.2 Morphology and particle size.

The properties of nanomaterials depend on their particle size.[50] To determine the particle size of the nanocrystals obtained, we used X-ray diffraction data and the Scherrer's equation[51], which describes the dependence of the broadening of the diffraction peak on the crystalline size.[52] Table 2 lists the particle size determined in this way.

Table 2. Nanoparticles size determined by the Scherrer's equation.

Nanoparticle	NPs size (nm)
3 at. % $KGd(WO_4)_2$	63.22*
5 at. % $NaGdF_4$ (method A)	41.71**
5 at. % $NaGdF_4$ (method B)	24.30**

*Calculated from the (220), (-222) and (002) peaks of the XRD patterns.
**Calculated from the (100), (110) and (101) peaks of the XRD patterns.

TEM images of these samples give information about the size distribution and morphology of the Nd^{3+} doped nanoparticles obtained. Figure 6 shows several TEM pictures of these nanoparticles recorded at different magnifications. The particles were agglomerated with a non-defined shape and with a high variety of sizes ranging from 2 µm to 6 µm. It was possible to observe the smaller particles, which were forming those big aggregates, with sizes between 70-150 nm in the case of 3 at. % Nd^{3+}:$KGd(WO_4)_2$ nanoparticles, 40-190 nm in 5 at. % Nd^{3+}:$NaGdF_4$ nanoparticles (Method A) and 70-250nm in 5 at. % Nd^{3+}:$NaGdF_4$ nanoparticles (Method B).

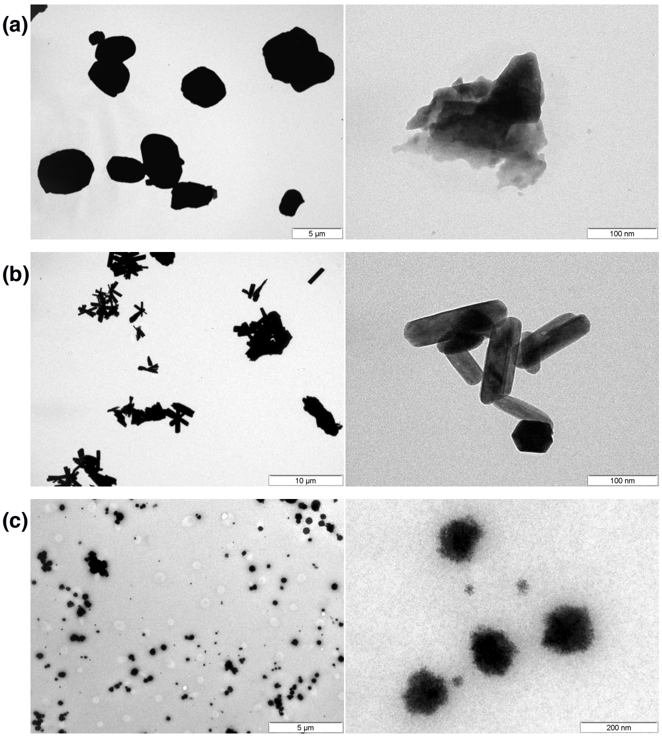

Figure 6.TEM images of: a) 3 at. % Nd^{3+}:$KGd(WO_4)_2$b) 5 at. % Nd^{3+}:$NaGdF_4$ (method A) and c) 5 at. % $Nd^{3+}NaGdF_4$ (method B) nanoparticles.

3.3 Reflectance measurements

Comparing the reflectance of both matrices doped with the maximum concentration of neodymium used, as can be observed in Figure 7, the presence of the characteristic bands of Nd^{+3} ions at around 750 and 900 nm (corresponding to the $^4F_{3/2} \rightarrow {}^4I_{9/2}$ and $^4F_{3/2} \rightarrow {}^4I_{11/2}$ transitions, respectively) is evidenced, confirming the doping of the nanoparticles with Nd^{3+}.

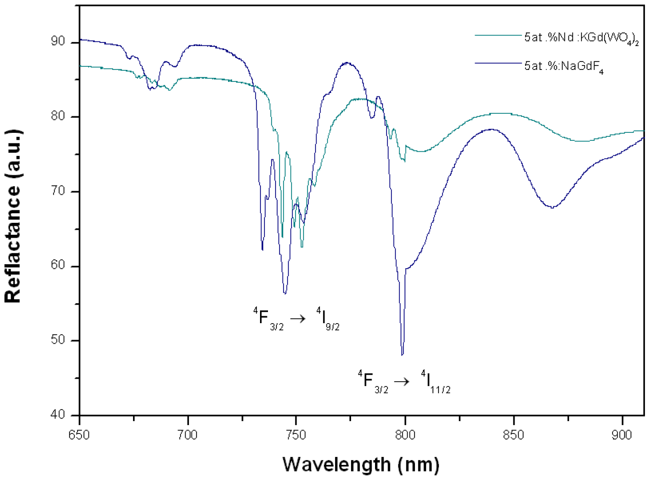

Figure 7.Reflectance spectra of 3 at. % Nd^{3+}:$KGd(WO_4)_2$ and 5 at. % Nd^{3+}: $NaGdF_4$ nanoparticles.

3.4 Luminescence Characterization

In this study, we optimized the percentage of Nd^{3+}, ranged between 1 at. % and 5 at. % that gives the maximum emission intensity, using the integrating sphere. The 3 at. % Nd^{3+}:$KGd(WO_4)_2$ nanocrystals showed the highest intensity in the NIR range, as can be seen in Figure 8 (a), and it was possible to observe the two multiplets corresponding to the $^4F_{3/2} \rightarrow {}^4I_{9/2}$ (~850 nm), and $^4F_{3/2} \rightarrow {}^4I_{11/2}$ (~1075 nm) transitions, as shown in Figure 8 (b). The first transition is located in the I-BW and the second transition lies in the desired II-BW. Among the transitions of Nd^{3+} we expected to obtain the emission corresponding to the $^4F_{3/2} \rightarrow {}^4I_{13/2}$ transition, around 1300 nm, lying again in the II-BW. However, as shown in Figure 8 (b), it was barely seen, since it is very weak, thus we will not be able to use this emission for thermometric purposes.

In this figure we also included an study of the efficiency of emission of the 3 at. % Nd^{3+}:$KGd(WO_4)_2$ nanoparticles synthesized using different C_M molar ratios, ranging form 0.16, corresponding to an EDTA molecule able to chelate 6 different metal atoms, to 1, corresponding to an EDTA molecule chelating only one metal atom. [53] The best results were obtained for C_M=1 allowing a better incorporation of the Nd^{3+} ions into the crystalline host.

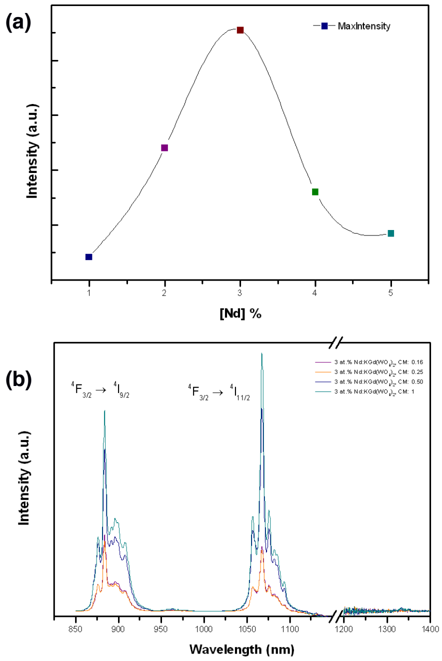

Figure 8. a) Evolution of the emission intensity of the $^4F_{3/2} \rightarrow {}^4I_{11/2}$transition in Nd^{3+}:$KGd(WO_4)_2$ nanoparticles as a function of the concentration of Nd^{3+}. b) Emission spectra of 3 at % Nd^{3+}:$KGd(WO_4)_2$ nanoparticles synthesized with different C_M ratios.

Figure 9 (a) shows the evolution of the intensity of the emission in the NIR for Nd^{3+}:$NaGdF_4$ nanocrystals with the concentration of Nd^{3+}. In that case, the particles that show the maximum intensity where those containing 5 at % Nd^{3+}. However, when compared this emission to that of 3 at % Nd^{3+}:$KGd(WO_4)_2$, the latter showed a more intense emission, as can be seen in Figure 9 (b), probably due to the large absorption cross section of this material .[54]

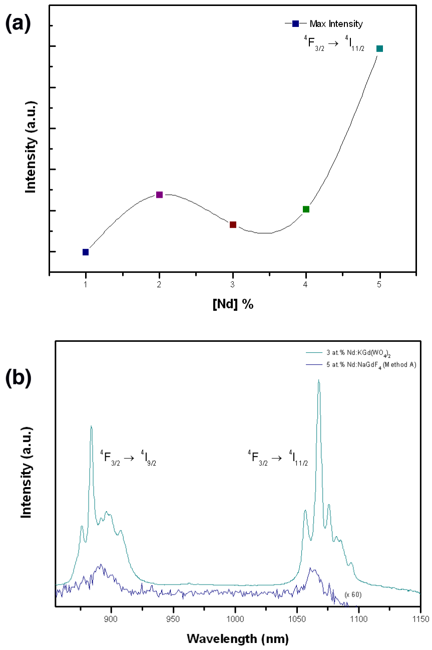

Figure 9. a) Evolution of the emission intensity of the$^4F_{3/2} \rightarrow {}^4I_{11/2}$ transition in Nd^{3+}:$NaGdF_4$ nanoparticles synthesized by method A, as a function of the Nd^{3+} concentration b) Comparison of emission spectra of 3 at % Nd^{3+}:$KGd(WO_4)_2$ and Nd^{3+}:$NaGdF_4$ synthesized by method A.

3.5 Thermometry Characterization.

To know the potential use of 3 at. % Nd^{3+}:KGd$(WO_4)_2$ nanoparticles for thermal sensing, it requires an adequate knowledge of the thermal response of the intensity of luminescence bands. Figure 10 (a) shows the emission spectra obtained from the 3 at. % Nd^{3+}:KGd$(WO_4)_2$ nanoparticles at two different temperatures (298 and 333 K) within the physiological range. The change in the intensity of emission induced by temperature is observed in the two most intense peaks, at around 883 nm and 1067 nm, as can be seen in detail in the insets.

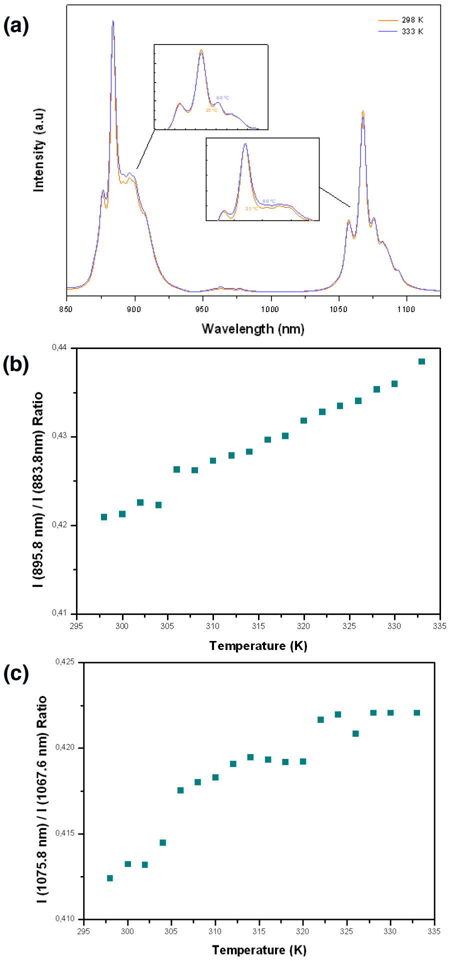

Figure 10. a) Normalized emission spectra of 3 at. % Nd^{3+}:KGd$(WO_4)_2$ nanoparticles at two different temperatures (298 and 333 K). b) Temperature variation of the ratio between the emitted intensities at 883 nm and 895 nm in the $^4F_{3/2} \rightarrow {}^4I_{9/2}$ transition. c) Temperature variation of the ratio between the emitted intensities at 1067 nm and 1075 nm in the $^4F_{3/2} \rightarrow {}^4I_{11/2}$ transition.

This allowed us to calculate two different intensity ratios, corresponding to the two emission bands recorded for Nd^{3+}, one lying in the I-BW, and the second one lying in the II-BW. For the $^4F_{3/2} \rightarrow {}^4I_{9/2}$ transition, we used the ratio between the emission peaks located at 883.8 nm and 895.8 nm (see Figure 10 (b)), while for the $^4F_{3/2} \rightarrow {}^4I_{11/2}$ transition, the ratio used was between the emission peaks located at 1067.6 nm and 1075.8 nm (see Figure 10 (c)). The intensity ratios in both cases presented a linear behavior in the intensity change, the first one with a slope of 0.02, while the second one showed a slower slope of 0.01. Also, we have estimated a thermal sensitivity (S), which is defined as the rate of change of the ratio with temperature. The one corresponding to the I (895.8 nm)/I (883.8 nm) ratio was ranged from 1.25 x 10^{-3} K^{-1} at 298 K to 1 x 10^{-3} K^{-1} at 333 K, and the I (1075.8 nm)/ I (1067.6 nm) ratio, the range became from 0.72 x 10^{-3} K^{-1} at 298 K to 0.58 x 10^{-3} K^{-1} at 333 K.

Therefore we obtained 1.25 x 10^{-3} K^{-1} at 298 K as the highest thermal sensitivity, which is very similar to the thermal sensitivities reported for other luminescent NTMs operating in the I-BW such as Nd^{3+}:$NaYF_4$[55] that presents 1.2 x 10^{-3} K^{-1} at 273 K thermal sensitivity. However, S reported here is minor from once already published for Nd^{3+}:YAG[56] and Nd^{3+}:LaF_3[19], which reported thermal sensitivities of 1.5 x 10^{-3} K^{-1} and 2.5 x 10^{-3} K^{-1}, respectively. Still, these nanothermometers only work in the I-BW while the 3 at. % Nd^{3+}:KGd(WO_4) synthesized nanoparticles can work in II-BW with a S = 0.072 x 10^{-2} K^{-1} at 298 K. Although its thermal sensitivity is not as high as the one reported for Nd^{3+}:$NaGdF_4$ + CdS/PbS/ZnS @ PLGA hybrid nanoparticles,[57] which have a thermal sensitivity corresponding to 2.5 x 10^{-2} K^{-1} at 303 K. This means that the thermal sensitivity of Nd^{3+}:KGd(WO_4) synthesized nanoparticles is the first one described in this biological window for a single type of nanoparticles.

3.6 Surface functionalization of the Nd^{3+}:KGd$(WO_4)_2$ nanoparticles.

As mentioned above it is very important to make the nanoparticles dispersible in an aqueous medium. To do that, we explored the silanization reaction. We used two washing solvents, ethanol and acetone. However, when we used acetone, we observed a larger agglomeration degree of the nanoparticles, the appearance of foam, and a color change in the surfactant at the end of the functionalization process. Thus, we decided to use only ethanol as the washing solvent. We also observed that by reducing the quantity of silane, we could get a larger degree of deaglomeration.

In Figure 11, we show the evolution of the deaglomeration of the nanoparticles in the most significant experiments. As we can see in Figure 11 (a), corresponding to conditions of Exp. 1 in Table 1, the nanoparticles form big aggregates, with sizes between 80-300 nm, but the presence of silane did not permit a correct dispersion. In Exp. 3, the dispersion of sizes of the aggregates is larger, 70-900 nm, (see Figure 11 (b)) due the use of acetone. In Exp. 9, we could not observe the presence of silane, and the particles still form big aggregates with sizes around 200-700 (see Figure 11 (c)). Finally, when the amplification of the ultrasounds was fixed at 35%, and we increased the pulse duration to 3 seconds and the amount of nanoparticle was reduced to a quarter part of the initial amount used, corresponding to the conditions of Exp.10 as listed in Table 1, the best results obtained, with nanoparticles fully dispersed with a mean size of 16 nm.

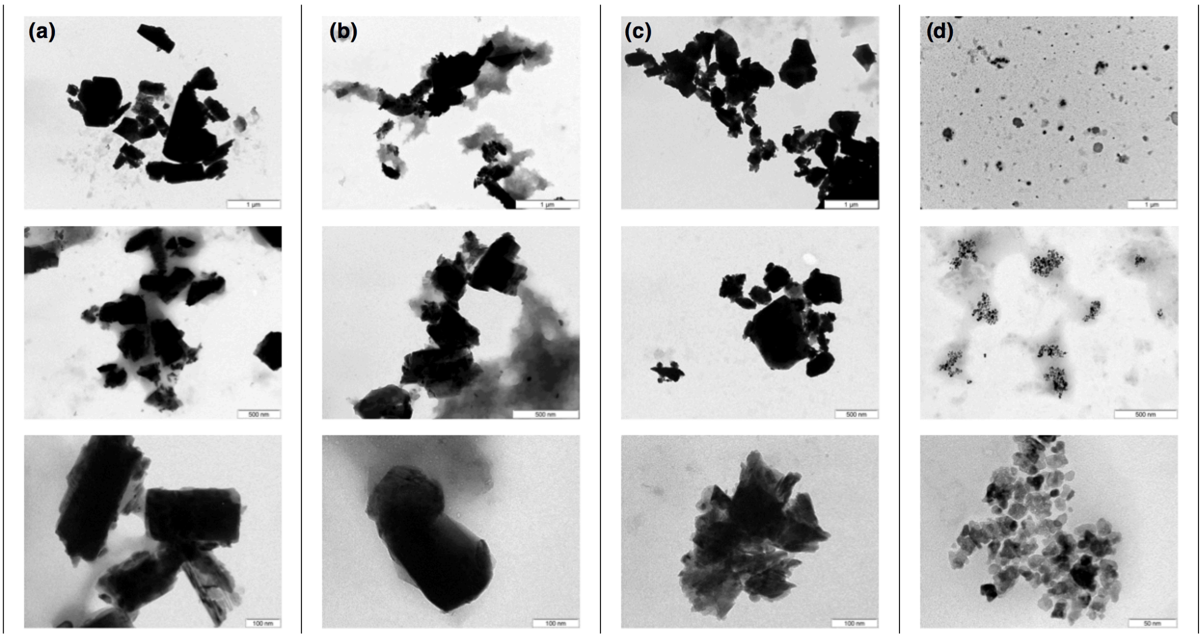

Figure 11. TEM images of the Nd^{3+}:$KGd(WO_4)_2$ nanoparticles with their surfaces fuctionalizated by silanization using different conditions as listed in Table 1. a) Exp.1, b) Exp.3, c) Exp.9 and d) Exp.10.

3.7 Sedimentation study

The sedimentation time is a very important characteristic to take into account in the dispersion of the nanoparticles, since dispersions are unstable from a thermodynamic point of view; however, they can be kinetically stable over a large period of time, which determines their shelf life.[58]

To analyze the sedimentation of our functionalized nanoparticles, different photographs of the vials containing the Nd^{3+}:$KGd(WO_4)_2$ nanoparticles dispersed in distilled water were recorded immediately after sonication and later on after 20 min., 30 min. and 40 min.. Results are shown in Figure 12.

Figure 12 (a) shows the photographs of Nd^{3+}:$KGd(WO_4)_2$ nanoparticles functionalized with silane molecules under the conditions of Exp. 1 in Table 1. Figure 12 (b) shows the nanoparticles washed with acetone (Exp. 3 in Table 1), in which we can observe the formation of foam and the change of color of the surfactant, passing from white to brown with a thick consistency. However, when compared to Exp. 1, the sedimentation time is extended (see Figure 12 (a)).

As we observed in TEM images, the reduction of the silane quantity helps to get a larger degree of deaglomeration of the nanoparticles, thus a greater dispersion was obtained in the same period of time, as we can observed in the last image of the Figure 12 (c), corresponding to Exp. 9. Thus, those results indicate that although we were not able to observe the presence of silane in the TEM images corresponding to this experiment, the nanoparticles have more stability in water, and do not sediment as fast as in the previous cases, indicating that a very thin layer of silane molecules is covering the particles. As mentioned previously, the best results in terms of dispersibility were obtained under the conditions of Exp. 10. However, due to the small amount of nanoparticles we obtained under these conditions made not possible to observe their sedimentation time.

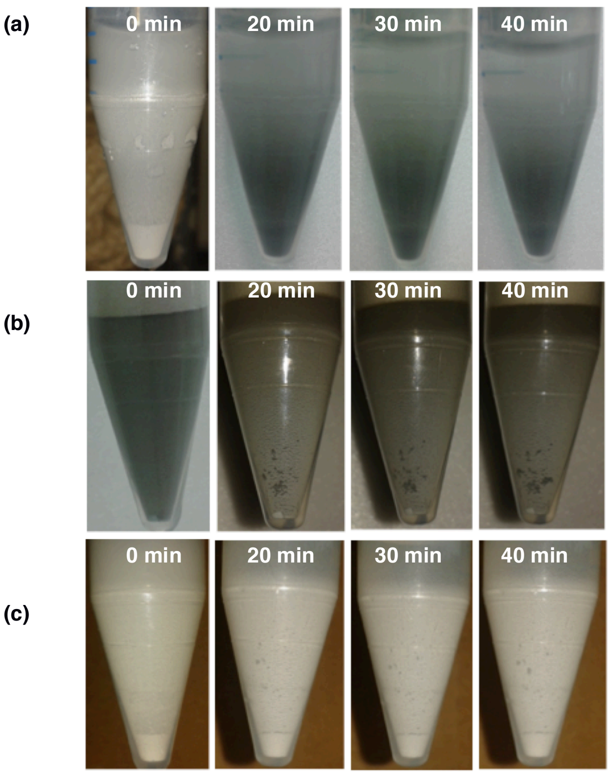

Figure 12. Sedimentation evolution with time of Nd^{3+}:$KGd(WO_4)_2$ nanoparticles functionalized by silanization. a) Exp. 1, b) Exp.3 and c) Exp.9 as listed in Table 1.

4 CONCLUSIONS

In summary, we performed an investigation of the luminescence properties of Neodymium doped $KGd(WO_4)_2$ and $NaGdF_4$ nanoparticles. Under infrared (808 nm) optical excitation, The Nd^{3+} doped nanoparticles show intense emissions bands at around 883 nm and 1067 nm corresponding to the ${}^4F_{3/2} \rightarrow {}^4I_{9/2}$ and ${}^4F_{3/2} \rightarrow {}^4I_{11/2}$ transitions, lying in the I- and II-BW, respectively.

The optimum doping conditions were 3 at. % of Neodymium in $KGd(WO_4)_2$, which showed the highest emission intensity. The thermal characterization of the luminescence properties of these nanoparticles indicate that they can be used as luminescent nanothermometers in the I- and II-BW. When working in the I-BW, the thermal sensitivity of our nanoparticles similar to the previously reported.[52] When operating in the II-BW, despite the thermal sensitivity is not as high as that reported for Nd^{3+}:$NaGdF_4$ + CdS/PbS/ZnS @ PLGA hybrid nanoparticles[54], it is the first time that thermal sensitivity is reported in this biological window using a single type of nanoparticles. Added to this, the dispersion of the nanoparticles we achieved when functionalized with silane molecules, indicate that these nanoparticles can be potentially used in-vivo tests, due to their small sizes of approximately 16 nm, which prevent their sedimentation in blood vessels.

ACKNOWLEDGEMENTS

This work was supported financially by FiCNA-FiCMA research group. And also thanks to Gemma Marsal for the assistance and support during development of this work.

REFERENCES

1. Jaque et al., Luminescence nanothermometry, *Nanoscale* **4**, 4301- 4326 (2012).

2. Brites et al., Thermometry at the nanoscale, *Nanoscale* **4**, 4799-4829 (2012).

3. L. Y. Ang et al., Applications of upconversion nanoparticles in imaging, detection and therapy, *Nanomedicine* **6**, 1273-1288 (2011).

4. A. M. Stark et al.,The use of thermovision in the detection of early breast cancer, *Cancer* **33**, 1664-1670 (1974).

5. J. Lee, N. A. Kotov, Thermometer design at the nanoscale, *Nano Today* **2**, 48-53 (2007).

6. E. Ring, The historical development of temperature measurementt in medicine. *J. Infrared Phys. Technol.* **49**, 297-301 (2007).

7. O. S. Wolfbeis, Lanthanide luminescence photophysical, analytical and biological aspects, *Springer series on fluorescence* **7** (2011).

8. Vetrone et al., Temperature sensing using fluorescent nanothermometers, *AcsNano* **4**, No. 6, 3254-3258 (2010).

9. X. Chen et al., Lanthanide-doped luminescent nanomaterials from Fundamental to bioapplications, *Springer* (2014).

10. G. K. Attanayake, Development of highly luminescent and water-dispersible lanthanide based nanomaterials for potential bio-medical imaging, Western Carolina University, Master thesis (2013).

11. M. Méndez, Synthesis and characterization of downshifting Ln^{3+} doped lanthanum-based nanoparticles for photovoltaic applications, Universitat Rovira i Virgili, Doctoral thesis (2013).

12. 13. P.R. Diamente et al., Water-soluble Ln^{3+-}doped LaF_3 nanoparticles: Retention of strong luminescence and potential as biolabels, *J.of Fluorescence* 15, No. 4 (2015).

13. Dong et. Al., NIR-to-NIR two-photon excited CaF_2:$Tm^{3+,}Yb^{3+}$ nanoparticles: multifunctional nanoprobes for highly penetrating fluorescence bio-imaging, *AcsNano* **5**, No.11, 8665-8671 (2011).

14. J.V, Frangioni, In vivo near-infrared fluorescence imaging, *Curr. Opin. Chem. Biol.* **7**, 626-634 (2003).

15. Marquez et al., Anisotropic absorption and reduced scattering spectra of chicken breast tissue measured using oblique incidence reflectrometry, *Applied Optics* **37**, No. 4, 798-804 (1998).

16. Smith et al., Bioimaging: second window for in vivo imaging, *Nat. Nanotechnol.* **4**, No. 11, 710-711 (2009).

17. R. Weissleder, A clearer vision for in vivo imaging, *Nat. Biotechnol.* **19** , 316 -317 (2001) .

18. U. Rocha et al., Neodymium-doped LaF_3 Nanoparticles for fluorescence bioimaging in the second biological window, *Small* **10**, No.6, 1141-1154 (2014).

19. U. Rocha et al., Subtissue thermal sensing based on Neodymium-doped LaF3 nanoparticles, *AcsNano* **7**, No. 2, 1188-1199 (2013).

20. Welsher et al., Deep-tissue anatomical imaging of mice using carbon nanotube fluorophores in the second near-infrared window, *Proc. Natl. Acad. Sci.* **108**, No. 22, 8943-8948 (2011).

21. Naccache et al., High-resolution fluorescence imaging of cancers using lanthanide ion-doped upconverting nanocrystals, *Cancers* **4**, 1067-1105, (2012).

22. Chatterjee et al., Upconversion fluorescence imaging of cells and small animals using lanthanide doped nanocrystals, *Biomaterials* **29**, 937–943 (2008).

23. F. Wang, X. Liu, Recent advances in the chemistry of lanthanide-doped upconversion nanocrystals, *Chem. Soc. Rev.* 38, 976–989 (2009).

24. An et al., Down-/up-conversion luminescence nanocomposites for dual-modal cell imaging. J. *Mater. Chem.* **1,** 1333–1339 (2013).

25. Liu, et al., A strategy to achieve efficient dual-mode luminescence of Eu^{3+} in lanthanides doped multifunctional

$NaGdF_4$ nanocrystals, *Adv. Mater.* **22,** 3266–3271 (2010).

26. Kumar et al., Combined optical and MR bioimaging using rare earth ion doped NaYF4 nanocrystals. *Adv. Funct. Mater.* **19**, 853–859 (2009).

27. J. Chen, J. X. Zhao, Upconversion Nanomaterials: Synthesis, Mechanism, and applications in sensing**,** *Sensors* **12***,* 2414-2435 (2012).

28. Yang et al. One-step hydrothermal synthesis of carboxyl-functionalizated upconversion phosphors for bioapplications *Chem. Eur. J.* **18**, 13642-13650 (2012).

29. G. Jiang et al., Neodymium doped lanthanum oxysulfide as optical temperature sensors, *J. of Luminescence* **152**, 156–159 (2014).

30. D. Jaque et al., Fluorescent nanoparticles for multi-photon thermal sensing, *J. of Luminescence* **133**, 249–253 (2013).

31. Zhang et al., Tunable photoluminescence and energy transfer of $YBO_3:Tb^{3+}$, Eu^{3+} for white light emitting diodes, *J. Mater. Chem.* **1**, 7202–7207 (2013).

32. Zhang et al., Synthesis and photoluminescence properties of hierarchical architectures of $YBO_3:Eu^{3+.}$ J. *Mater. Chem.* **22**, 6485–6490 (2012).

33. Zhang et al., Hydrothermal synthesis and luminescent properties of $LaPO_4$:Eu 3D microstructures with controlable phase and morphology. *Mater. Res. Bull.* **45**, 1324-1329 (2011).

34. Liu et al. Covalently assembled NIR nanoplatform for simultaneous fluorescence imaging and photodynamic therapy of cancer cells, *ACS Nano* **6**, 4054–4062 (2012).

35. Pokhrel et al., Stokes emission in $GdF_3:Nd^{3+}$ nanoparticles for bioimaging probes, *Nanoscale* **6**, 1667–1674 (2014).

36. Li et al., Nd3+ sensitized up/down converting dual-mode nanomaterials for efficient in vitro and in vivo bioimaging excited at 800 nm. *Sci. Rep.* **3**, No. 3536 (2013).

37. Deloach et al., Evaluation of absorption and emission properties of Yb^{3+} doped crystals for laser applications, *Quantum Electron*. **29**, No. 4, 1179-1191 (1993).

38. W.F. Krupke, Ytterbium solid-state lasers, *Quantum Electron* **6**, 1287–1296, (2000).

39. M. C. Pujol et al., Structural study of monoclinic $KGd(WO_4)_2$ and effects of lanthanide substitutions, *J.Appl.Cryst.***34**, 1-6 (2001).

40. J. Chen, J. X. Zhao, Spectroscopic properties of $KGd(WO_4)_2$ and $KGd(WO_4)_2:Ho^{3+}$ single crystals studied by brillouin and raman scattering methods, *Sensors* **12**, 2414-2435 (2012).

41. Petrov et al., Efficient tunable laser operation of $Tm:KGd(WO_4)_2$ in the Continuous-Wave Regime at Room Temperature, *Quantum Electronics* **40**, No. 9, 1244-1251 (2004).

42. Wang et al., Pure near-infrared to near-infrared upconversion of multifunctional Tm^{3+} and Yb^{3+} co-doped $NaGd(WO_4)_2$ nanoparticles, *J. Mater. Chem. C.* **2**, 4495-4501 (2014).

43. G. Chen et al., Core/Shell $NaGdF4:Nd_3/NaGdF_4$ nanocrystals with efficient near-infrared to near-infrared downconversion photoluminescence for bioimaging applications, *ASC Nano* **6**, No. 4, 2969-2977 (2012).

44. C. Mi et al., Synthesis of surface amino-functionalized $NaGdF_4$:Ce,Tb nanoparticles and their luminescence resonance energy transfer (LRET) with Au nanoparticles, *Colloids and surfaces A: Physicochem. Eng. Aspects* **395**, 152-156 (2012).

45. Zhang et al. Magnetic and optical properties of $NaGdF_4:Nd^{3+}$, Yb^{3+}, Tm^{3+} nanocrystals with upconversion/downconversion luminescence from visible to the near-infrared second window. *Nano Researh* **8**, No. 2, 636-648 (2015).

46. Zhou et al., Dual-modality in vivo imaging using rare-earth nanocrystals with near-infrared to near-infrared (NIR-to-NIR) upconversion luminescence and magnetic resonance properties, *Biomaterials* **31,** 3287–3295 (2010).

47. Thangaraju et al., Synthesis and characterization of monoclinic $KGd(WO_4)_2$ particles for non-cubic transparent ceramics, *Optical Materials* **35,** 753–756 (2013).

48. Ding et al., Simultaneous morphology manipulation and upconversion luminescence enhancement of β-$NaYF_4:Yb^{3+}/Er^{3+}$ microcrystals by simply tuning the KF dosage, *Scientific Reports* (2015).

49. Z. Wang et al., Down and upconversion photoluminescence, cathodoluminescence and paramagnetic properties of $NaGdF_4:Yb^{3+}$, Er^{3+} submicrondisks. *J. Mater. Chem*. **20**, 3178–3185 (2010).

50. R. Vajtai, Handbook nanomaterials , *Springer* (2013).

51. A. Monshi, M. Reza, Modified scherrer equation to estimate more accurately nano-crystallite size using XRD. *World Journal of Nano Science and Engineering* **2**, 154-160 (2012).

52. A. Leroy , H. Klug, Determination of crystallite size with the x-ray spectrometer. *Journal of Applied Physics* **21**, 137-143 (1950).

53. D. A. Skoog , D. M. West, Fundamentals of Analytical Chemistry (2013).

54 . X. Wu, L. Cheng, Structure-property relationships in non-linear optical crystals II, *Springer* (2012).

55 . Wawrzynczyk et al. Luminescent nanoprobes for thermal bio-sensing: Towards controlled photo-thermal therapies, *Nanoscale* **4**, 6959–6961, (2012).

56. Vetrone et al., Nd-YAG near-infrared luminescent Nanothermometers, *Adv. Optical. Mater*. (2015).

57. Jaque et al., Hybrid Nanostructures for High-Sensitivity Luminescence Nanothermometry in the Second Biological Window, *Adv. Mater.* **27**, 4781–4787 (2015).

58. E. Kissa, Dispersions: Characterization, Testing, and Measurement, *Surfactant Science Series* **84**, (1999).